Broadband dielectric response and grain-size effect in $K_{0.5}Na_{0.5}NbO_3$ ceramics

E. Buixaderas,[1,a)] V. Bovtun,[1] M. Kempa,[1] M. Savinov,[1] D. Nuzhnyy,[1] F. Kadlec,[1] P. Vaněk,[1] J. Petzelt,[1] M. Eriksson,[2] and Z. Shen[2]
[1]*Department of Dielectrics, Academy of Sciences of the Czech Republic, Na Slovance 2, 182 21 Prague 8, Czech Republic*
[2]*Department of Inorganic Chemistry, Arrhenius Laboratory, Stockholm University, S-106 91 Stockholm, Sweden*

(Received 11 September 2009; accepted 14 November 2009; published online 15 January 2010)

Dielectric spectra of two $K_{0.5}Na_{0.5}NbO_3$ ceramics with different grain sizes (10 and 0.5 μm) were measured from 10^2 to 10^{14} Hz in a broad temperature range. The sequence of first-order phase transitions (cubic-tetragonal-orthorhombic-rhombohedral) was detected by differential scanning calorimetry, dielectric spectroscopy, and time-domain terahertz spectroscopy. The grain size affects all the phase transitions, which are more smeared in the small-grain sample. In the large-grain ceramics, two well-separated near-Debye relaxations are seen in the tetragonal phase, which suddenly merge on cooling across the tetragonal-orthorhombic transition, and on further cooling the lower-frequency relaxation strongly broadens. On reducing the grain size, the higher-frequency relaxation shifts from ~1 to ~20 GHz and the lower-frequency one strongly broadens. Without quantitative understanding, these effects could be assigned to domain-wall dynamics and its temperature and grain-size dependences. Similar to pure $KNbO_3$, an overlapped central-mode–soft-mode type excitation was detected in the terahertz range related to the effective hopping and oscillations of the off-centered Nb ions in a multiwell potential. © *2010 American Institute of Physics*. [doi:10.1063/1.3273490]

I. INTRODUCTION

Sodium potassium niobate $K_xNa_{1-x}NbO_3$ (KNN) is a promising candidate for replacing $Pb(Zr_xTi_{1-x})O_3$ in piezoelectric devices as a lead-free material. The addition of $KNbO_3$ to antiferroelectric $NaNbO_3$ induces ferroelectricity already in the high-temperature tetragonal phase and suppresses the appearance of the sequence of four orthorhombic phases on lowering the temperature.[1] Ceramics based on $NaNbO_3$ and $KNbO_3$ exhibit very high piezoelectric coefficients due to the piezoelectric properties of both parent materials.[2,3] Moreover, enhanced piezoelectric and dielectric properties are found in the morphotropic phase boundary composition $(K_{0.5}Na_{0.5})NbO_3$ (KNN-50) due to coexistence of orthorhombic and tetragonal domains.[4] KNN-50 shows the same behavior as $KNbO_3$ or $BaTiO_3$, but with all phase transitions (PTs) shifted to lower temperatures.[5] The sequence of PTs follows the pattern of $BaTiO_3$: From the high-temperature cubic phase, KNN-50 goes through tetragonal, orthorhombic, and finally rhombohedral phases.[6] These PTs were studied in detail by dielectric and spectroscopic methods on $KNbO_3$ single crystals,[6–8] but much less work was done on KNN ceramics[9] or powders.[10]

The spectroscopic characterization of KNN-50 ceramics was performed recently by some of us using Raman, infrared (IR), and time-domain terahertz (TDTHz) techniques.[11,12] It was found that the three PTs exhibit first-order character, especially the lowest-temperature one near 90 K, below which all the Raman modes under 100 cm^{-1} disappear. It was shown that an overdamped soft mode (triply degenerate) is present in the terahertz (THz) range at high temperatures. On cooling, the soft THz mode reduces its dielectric strength at each PT (when one component stiffens and shifts to higher frequencies and the corresponding vector of the spontaneous polarization appears) and finally disappears from the THz range abruptly when entering the rhombohedral phase. Comparison of these results with the low-frequency dielectric data (0.1–1000 kHz)[1,13] indicates another dispersion below the polar phonon frequencies (presumably in the microwave range) which is needed to explain the static value of the permittivity.

It is known that the grain size affects the dielectric behavior of the ferroelectric $BaTiO_3$ in the microwave range,[14] related to the presence of ferroelectric and ferroelastic domains. A similar behavior is expected for $KNbO_3$ and KNN ceramics. In this paper, we report a detailed temperature dependent dielectric study of KNN-50 ceramics with different grain sizes in a very broad frequency range (10^2–10^{14} Hz). We also discuss the nature of the main dielectric contributions and the influence of the grain size on the dielectric properties.

II. EXPERIMENTAL

KNN samples were prepared by spark plasma sintering (SPS) in a furnace (Dr. Sinter 2050, SPS Syntex Inc., Japan) using commercial $Na_{0.5}K_{0.5}NbO_3$ powder (Ferroperm, Denmark, provided by St Jude Medical AB, Järfälla, Sweden) with an initial particle size of ~200 nm. The powder was loaded into a graphite die with an inner diameter of 12 mm.

a)Electronic mail: buixader@fzu.cz.

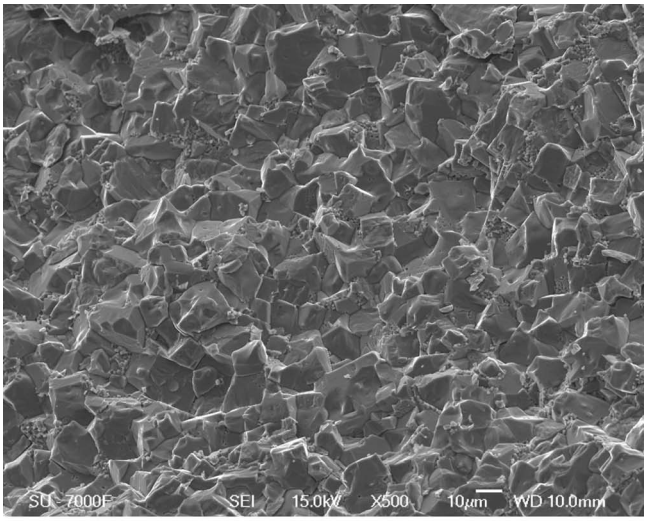

(a)

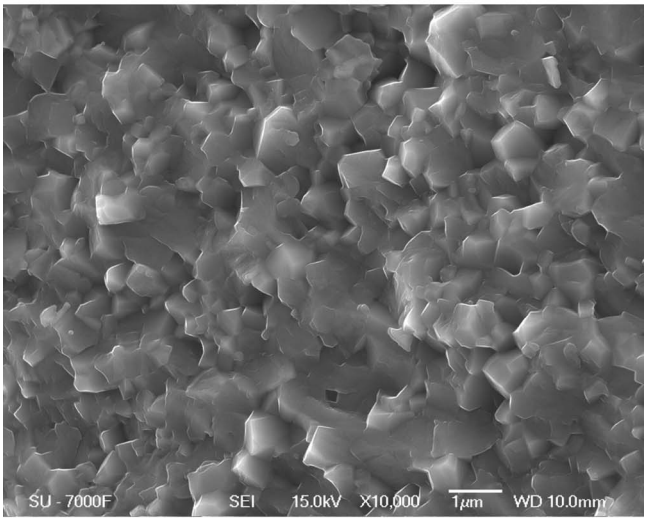

(b)

FIG. 1. SEM pictures of the KNN-50 samples: (a) large grain and (b) small grain. Note the different scales.

The sintering temperature was controlled by a pyrometer focused on the die surface. Resulting density was about 99% of the theoretical value. More details are given elsewhere.[15] Two kinds of ceramics with different grain sizes were prepared: the large-grain (about 10 μm) ceramic was obtained by sintering at 1000 °C for 3 min, and the small-grain (about 0.5 μm) ceramic obtained by sintering at 850 °C for 5 min. Then both ceramics were annealed in air at 800 °C for 6 h, and in addition the large-grain sample was also annealed at 900 °C for 8 h to reduce the defect level. The resulting microstructure of both ceramics was analyzed by scanning electron microscopy (SEM) and is shown in Fig. 1.

Differential scanning calorimetry (DSC) measurements were performed with a Perkin-Elmer Pyris Diamond calorimeter (temperature range of 298–723 K) and Perkin-Elmer DSC7 calorimeter (temperature range of 93–323 K) on heating with a rate of 10 K/min. The temperature calibration for high-temperature measurements was performed on heating using extrapolated onsets of melting peaks of water, indium, and zinc. The heat flow was calibrated using the melting enthalpy of indium. Temperature calibration for the low-temperature measurements was performed using extrapolated onsets of melting peak of cyclohexane and PT of cyclohexane. The heat flow was calibrated using the melting enthalpy of cyclohexane. Samples of prismatic shape (masses of 81 and 87 g for large and small-grain ceramics, respectively) were hermetically closed in aluminum pans. in the temperature range 298–723 K for high-temperature measurements and without pans for low-temperature ones. Each sample was measured at least twice. The measurements were controlled and evaluated using the PYRIS 4.02 software.

For dielectric experiments in the high-frequency range (10^6–10^9 Hz), cylindrical rod shaped samples of diameter d=0.95 mm and height h=6.0 mm were prepared. Computer controlled high-frequency dielectric spectrometer equipped with an Agilent 4291B impedance analyzer, a Novocontrol BDS 2100 coaxial sample cell, and a Sigma System M18 temperature chamber (operation range 100–570 K) were used. Impedance spectra of the samples with Au electrodes sputtered on the bases of the cylinders were recorded on cooling with the rate of 2 K/min. Frequency dependences of the dielectric permittivity (ε') and loss (ε'') were calculated accounting for the electromagnetic field distribution in the samples. Microwave measurements at 8.8 GHz were performed using a TE_{0n1} composite dielectric resonator[16] with an Agilent 58364B vector network analyzer in the temperature range 100–380 K at the rate of 1 K/min. The same samples used for high-frequency coaxial measurements were inserted in a hole at the center of the dielectric resonator. Dielectric parameters of the measured samples were extracted from analysis of the resonance curves measured with and without the sample.

For low-frequency dielectric measurements (10^2–10^6 Hz) with a Hewlett-Packard 4192A impedance analyzer, gold electrodes were sputtered onto the faces of 200 μm thick plates. Samples were heated and cooled in the temperature range 20–750 K with a rate of 2 K/min.

TDTHz transmission measurements were carried out on thin polished plane-parallel samples (~98 μm thick) in the temperature range 20–900 K. A custom-made TDTHz transmission spectrometer was used to obtain the complex dielectric response from 0.2 to 2 THz with a resolution of 0.05 THz. At higher frequencies, the samples were opaque. An Optistat CF cryostat with Mylar windows was used for measurements down to 20 K. Adapted commercial high-temperature cell SPECAC P/N 5850 was used to heat the samples up to 900 K.

IR reflectivity measurements at room temperature (RT) were performed on polished ceramic disks (7 mm diameter and 1 mm thick) using a Fourier transform IR spectrometer Bruker IFS 113v. Spectra were taken in the 30–3000 cm^{-1} range with a resolution of 2 cm^{-1} and using a DTGS pyroelectric detector.

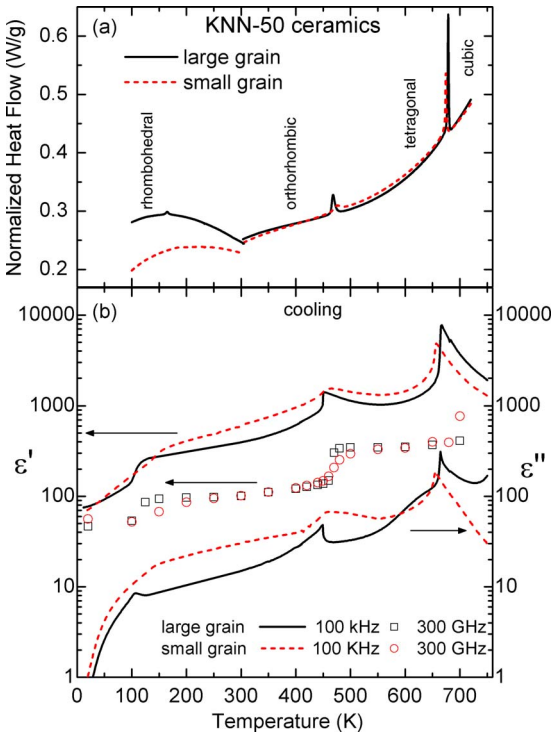

FIG. 2. (Color online) Characterization of the PTs in KNN-50 samples by (a) DSC and (b) dielectric measurements on cooling [lines—dielectric permittivity (ε') and loss (ε'') at 100 kHz; points—permittivity at 300 GHz].

III. EXPERIMENTAL RESULTS

A. DSC

Temperature dependences of the measured heat flows normalized to the mass of each sample are shown in Fig. 2(a) for both KNN-50 samples. Above RT two transitions were detected: from cubic to tetragonal phase (at T_{C1}=677 K and 673 K for the large and small-grain samples, respectively), and from tetragonal to orthorhombic phase (T_{C2}=464 K and 466 K for the large and small grains, respectively). Below RT a third PT was detected for the large-grain sample, from orthorhombic to rhombohedral phase (T_{C3}=165 K), but no transition was detected in the small-grain sample, just a weak change in slope near 180 K. Transitions are of the first order as deduced from the presence of peaks in the heat flow curves and follows from symmetry considerations for the ferroelectric-ferroelectric PTs, which are of no group-subgroup relation. The enthalpy change ΔH is almost twice larger for the large-grain sample (see Table I). Transition temperatures calculated as the extrapolated onsets and the calculated enthalpy changes are shown in Table I. Change in the grain size affects all the PTs in KNN-50. Peaks in the heat flow are smaller and broader for the small-grain ceramics [see Fig. 2(a)]. It is interesting to notice that the shifts of T_{C1} and T_{C2} caused by reduction in grain size are in opposite direction; therefore these transitions are closer to one another for the small-grain ceramics.

B. Dielectric spectroscopy (10^2–10^{10} Hz)

Low frequency dielectric measurements (10^2–10^6 Hz) were performed in a heating-cooling-heating cycle. Samples with larger grains showed substantial thermal hysteresis. Even after the annealing, the first heating showed strong anomalies. The shifts of dielectric anomalies related to T_{C2} and T_{C3} between heating and cooling were several tens of degrees for this sample. By contrast, in ceramics with smaller grains the thermal hysteresis was not so pronounced: permittivity values on cooling and heating were more alike and shifts in T_C were less than 10°. Anomalies of $\varepsilon'(T)$ at T_{C1} did not show important hysteresis.

The temperature dependences of the dielectric permittivity and loss at 100 kHz on cooling are depicted in Fig. 2(b) for both samples. Dielectric data are in agreement with the DSC measurements, except for a small shift in the transition temperatures. Temperatures at which maxima of the permittivity occur are shown in Table I. The cubic-tetragonal PT occurs at higher temperature in the large-grain sample, but T_{C2} and T_{C3} are lower. Their permittivity peaks are much broader in the small-grain sample. The third PT from orthorhombic to rhombohedral phase is almost not detected in the small-grain sample. The large-grain ceramics has higher permittivity and loss around T_{C1} but, otherwise, it shows lower values. Permittivity at 300 GHz measured with the TDTHz technique (see below) is also shown in Fig. 2 for comparison. The values of ε' at 300 GHz are mainly defined by the polar phonon dielectric contribution and are much smaller than the low-frequency ε'. It is clear that the main contribution to the permittivity (except for the lowest temperature) is due to the relaxation dispersion at frequencies below 300 GHz.

The results of the dielectric measurements at high and microwave frequencies (10^6–10^{10} Hz) are presented in Fig. 3, where the temperature dependences of the permittivity and loss for both samples are shown together with dielectric data at ~1 kHz and 500 GHz, from 100 to 500 K. The tetragonal to orthorhombic PT is clearly detected in both ceramics. In the large-grain ceramics [Fig. 3(a)], the maximum of the permittivity is much sharper than in the small-grain one, where a broader maximum is seen also in the dielectric loss [Fig. 3(b)]. Values of ε' and ε'' maxima at T_{C2} are lower for this sample. The PT to the rhombohedral phase was also detected

TABLE I. Summarizing results of the DSC experiment on KNN-50 ceramics with different grain sizes and permittivity maxima found in the low-frequency dielectric experiment.

KNN-50	Large grain				Small grain	
T_C (K) DSC	161.9	464.2	677	⋯	465.7	672.7
ΔH (J g^{-1})	0.19	1.5	3.0	⋯	0.67	2.0
T_C (K) ε'_{max} at 100 kHz	~117	452	667	~150	460	654

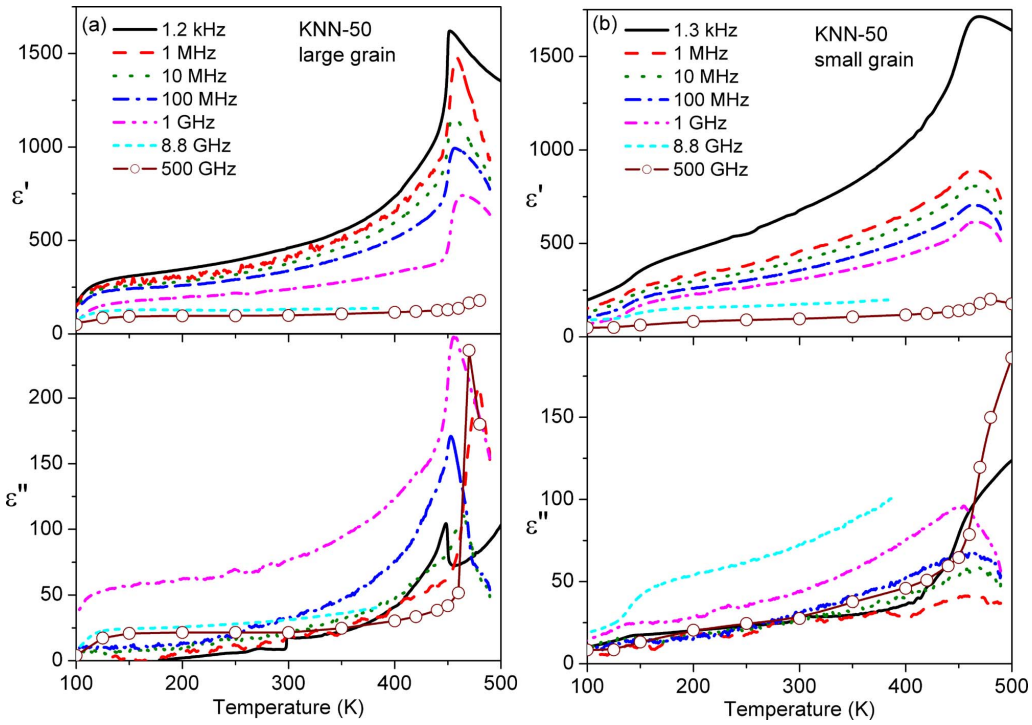

FIG. 3. (Color online) Temperature dependences of the dielectric permittivity (ε') and loss (ε'') at several frequencies on cooling of KNN-50 ceramics with large (a) and small (b) grains.

in both cases, but in the small-grain ceramics it occurs at higher temperatures (by several tens of degrees).

C. Terahertz and IR spectroscopies (10^{11}–10^{14} Hz)

Dielectric spectra in the THz range are plotted in Fig. 4. In the large-grain ceramics [Fig. 4(a)], both permittivity and loss decrease on cooling from the cubic phase. The three PTs are very well detected as jumps in the values of both ε' and ε'' (see Fig. 2). On the contrary, the small-grain ceramics [Fig. 4(b)] shows a more monotonic decrease in the ε' and ε'' values, and the PTs are smeared (Fig. 2).

IR reflectivity spectra at RT together with calculated reflectivity from the TDTHz data are presented in Fig. 5(a). The lower-frequency range in the linear scale is shown in the inset. The data above 50 cm^{-1} (1.67 THz) are from the IR experiment, while the data below 50 cm^{-1} are from the TDTHz experiment. It is clear that no significant differences

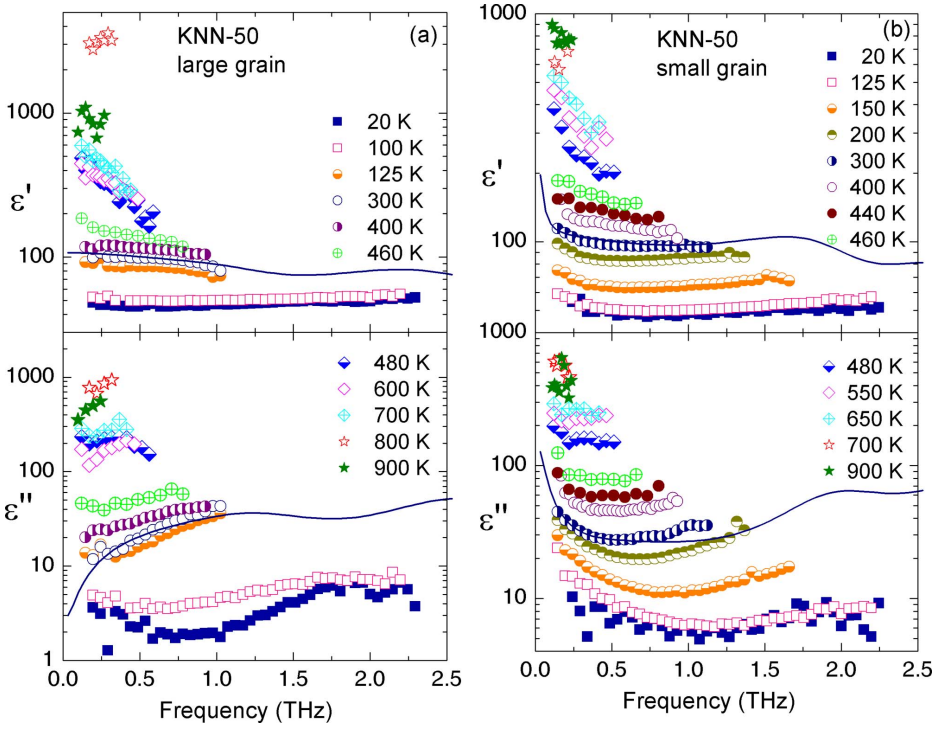

FIG. 4. (Color online) Frequency dependences of the dielectric permittivity (ε') and loss (ε'') in the THz range of KNN-50 ceramics with large (a) and small (b) grains at different temperatures. The solid lines correspond to the IR fit at 300 K using Eqs. (1) and (2).

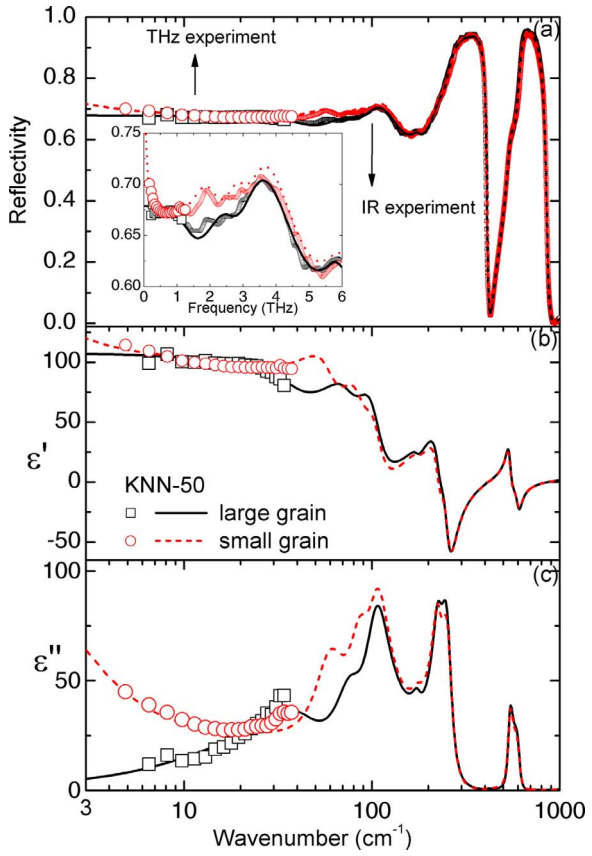

FIG. 5. (Color online) Reflectivity (a), dielectric permittivity (b), and loss (c) spectra of KNN-50 ceramics in the IR and THz ranges at RT (1 THz ~33 cm^{-1}). Symbols—experiment; lines—fits using Eqs. (1) and (2). Inset: Detail of the far-IR reflectivity region together with the calculated THz reflectivity points.

related to the grain size are seen in the IR range. Only below 100 cm^{-1}, the reflectivity is slightly lower in the large-grain ceramics, apparently due to the smaller influence of the relaxation excitations below phonon modes.

The IR reflectivity spectra were fitted together with the complex THz dielectric spectra using the factorized oscillator model of the complex permittivity (dielectric function) ε^*:[17]

$$\varepsilon^*(\nu) = \varepsilon'(\nu) - i\varepsilon''(\nu) = \varepsilon_\infty \prod_{j=1}^{n} \frac{\nu_{LOj}^2 - \nu^2 + i\nu\gamma_{LOj}}{\nu_{TOj}^2 - \nu^2 + i\nu\gamma_{TOj}}, \quad (1a)$$

$$\Delta\varepsilon_j = \frac{\varepsilon_\infty}{\nu_{TOj}^2} \frac{\prod_k (\nu_{LOk}^2 - \nu_{TOj}^2)}{\prod_{k\neq j} (\nu_{TOk}^2 - \nu_{TOj}^2)}, \quad (1b)$$

where ε_∞ is the permittivity at frequencies ν much higher than all polar phonon frequencies, ν_{TOj} and ν_{LOj} are the transverse and longitudinal frequencies of the jth phonon mode, and γ_{TOj} and γ_{LOj} are their respective damping constants. $\Delta\varepsilon_j$ refers to its dielectric contribution. The complex permittivity $\varepsilon^*(\nu)$ is related to the reflectivity spectrum $R(\nu)$ by

$$R(\nu) = \left| \frac{\sqrt{\varepsilon^*(\nu)} - 1}{\sqrt{\varepsilon^*(\nu)} + 1} \right|^2. \quad (2)$$

The permittivity and dielectric loss in the THz range together with the calculated one from the far-IR fit are shown at RT in Figs. 5(b) and 5(c) for both samples. The values of the THz permittivity are similar in both samples; however, dielectric losses of the small-grain ceramics show an increase below 10 cm^{-1}, which is caused by excitations at lower frequencies [see Fig. 2(b)]. We can conclude that the phonon dielectric contributions are similar in both KNN ceramics and the grain-size reduction has no essential influence on the phonon dynamics. Parameters of the fitted IR modes are shown in Table II. A more detailed study of the phonons in KNN-50 ceramics can be found in Refs. 11 and 12.

IV. DISCUSSION

The mechanism of the PTs in $KNbO_3$ is of mixed displacive-order-disorder type as from the point of dynamics analyzed by Fontana *et al.*[18] based on the previous dielectric spectroscopy and light scattering results. To explain the low-frequency dielectric data, they assumed an additional Debye relaxation in the cubic and tetragonal phases. The response in the cubic phase was then theoretically discussed by Girsh-

TABLE II. Parameters of the IR phonons used to fit the IR and THz spectra in Fig. 5 for both KNN-50 samples with Eqs. (1) and (2). ε_∞=4.8, ν_{TO}, and γ_{TO} are in cm^{-1}.

KNN-50									
Large grain					Small grain				
ν_{TO}	γ_{TO}	ν_{LO}	γ_{TO}	$\Delta\varepsilon$	ν_{TO}	γ_{TO}	ν_{LO}	γ_{TO}	$\Delta\varepsilon$
0.4	26.8	0.8	39.8	339.8	4.3	26.4	9.8	41.7	300.2
41.2	33.8	44.7	33.8	12.9	59.6	28.4	66.2	33.1	18.4
76.3	33.7	82.2	34.1	12.9	86.1	27.1	91.7	28.6	10.6
104.4	40.4	139.9	100.3	21.8	106.0	36.4	139.9	100.1	16.9
175.2	22.0	176.8	23.1	0.5	175.2	30.2	176.8	33.3	0.5
226.6	33.8	233.5	35.0	5.0	226.1	31.7	233.5	33.1	4.9
252.4	42.8	331.9	98.7	11.5	254.1	44.3	331.9	98.7	11.4
334.0	96.1	411.7	8.9	0.2	334.0	96.1	411.7	8.9	0.2
415.2	14.4	419.4	16.0	0.0	415.2	11.5	419.4	16.0	0.0
540.9	41.2	575.6	107.4	1.8	540.9	42.8	575.6	105.8	1.8
602.4	53.8	711.2	162.6	1.2	602.4	57.0	711.2	162.6	1.2
715.9	164.1	857.8	31.7	0.1	715.9	164.1	857.8	31.7	0.1

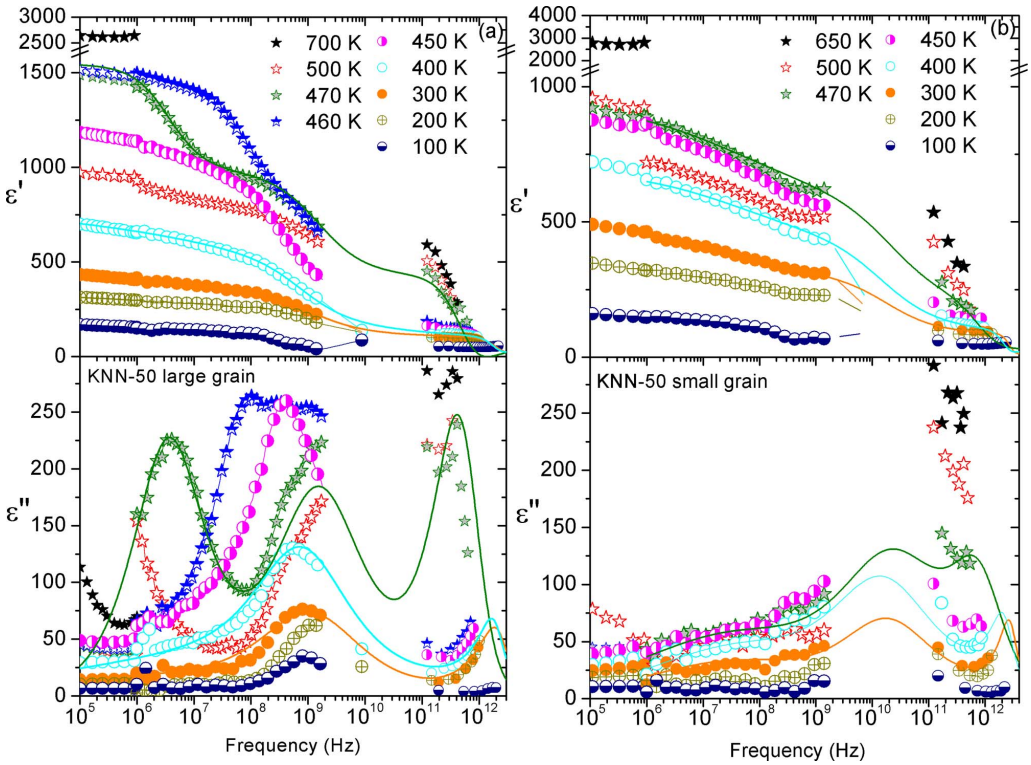

FIG. 6. (Color online) Frequency dependence of the dielectric permittivity (ε') and loss (ε'') of KNN-50 with large (a) and small (b) grains. Symbols—experiment; lines—fits with Eq. (3).

berg and Yacoby[19] and explained by an overlapped central-mode relaxation due to a fast hopping of the off-centered Nb ions and soft-mode oscillator, both in the THz range. The situation is very similar to that revealed recently in $BaTiO_3$.[20] The presence of soft phonon modes speaks in favor of the displacive type,[6,8] whereas the strong dynamic disorder caused by Nb atoms follows the pattern of order-disorder type PTs.[21,22]

Our previous investigations[11,12] have shown that in KNN, when entering into the orthorhombic phase, an excitation below polar phonon region appears (probably in the microwave range), which carries the most part of the dielectric permittivity. In order to quantify this excitation, all dielectric data were combined and fitted simultaneously. The complex permittivity $\varepsilon^*(\nu)$ in the megahertz (MHz) to THz range was modeled by two Cole–Cole relaxations and one heavily damped oscillator, representing in a simplified way the overlapped central+soft-mode response:

$$\varepsilon^*(\nu) = \varepsilon'(\nu) - i\varepsilon''(\nu) = \sum_{j=1}^{2} \frac{\Delta\varepsilon_j}{1 + (i\nu/\nu_j)^{1-\alpha_j}} + \frac{\Delta\varepsilon_{CM}\nu_{CM}^2}{\nu_{CM}^2 - \nu^2 + i\gamma_{CM}\nu} + \varepsilon_{IR}, \quad (3)$$

where $\Delta\varepsilon_j$ are the dielectric strengths of the Cole–Cole relaxations, ν_j is their mean relaxation frequencies, and α_j is a real index between 0 and 1, which determines the deviation from the pure Debye model and characterizes the width of the distribution of the Debye relaxation frequencies. $\Delta\varepsilon_{CM}$, ν_{CM}, and γ_{CM} denote the dielectric strength, frequency, and damping of the oscillator in the THz range, respectively. ε_{IR} stands for the dielectric contributions of phonons with frequencies higher than 2 THz.

Frequency dependences of the real and imaginary parts of the complex dielectric permittivity at different temperatures are presented in Fig. 6, for both large- and small-grain ceramics. It is well seen that their dielectric behavior differs strongly below 10 GHz. In the large-grain sample, the loss spectra contain rather narrow maxima, whose frequencies change with temperature [Fig. 6(a)]. These features are absent in the small-grain sample loss spectra, where much broader relaxations are observed [Fig. 6(b)].

In Fig. 7, the dielectric data in the high-frequency range for the large-grain sample are presented in a Cole–Cole plot. From this figure, it is clearly seen that two separate processes are present in this frequency range above T_{C2}. On cooling, they merge and below T_{C2} only one asymmetric peak is seen.

The fits performed with Eq. (3) for the large-grain sample are shown in Fig. 8 together with the experimental results for the permittivity and losses around the tetragonal-orthorhombic PT. The individual contributions of the two Cole–Cole relaxations and the oscillator in the THz range are also depicted. Similar fits were performed for the small-grain sample [at RT, 400 K, and 470 K they are shown in Fig. 6(b)].

Temperature dependences of the fit parameters for both samples are plotted in Fig. 9. The mean relaxation frequencies ν_1 and ν_2 as well as the frequency of the oscillator in the THz range ν_{CM} are depicted in the upper figures. Their contributions to the permittivity $\Delta\varepsilon_1$, $\Delta\varepsilon_2$, and $\Delta\varepsilon_{CM}$ are shown in the lower part together with the total contribution $\Sigma\Delta\varepsilon = \Delta\varepsilon_1 + \Delta\varepsilon_2 + \Delta\varepsilon_{CM} + \varepsilon_{IR}$ and the measured permittivity at 100

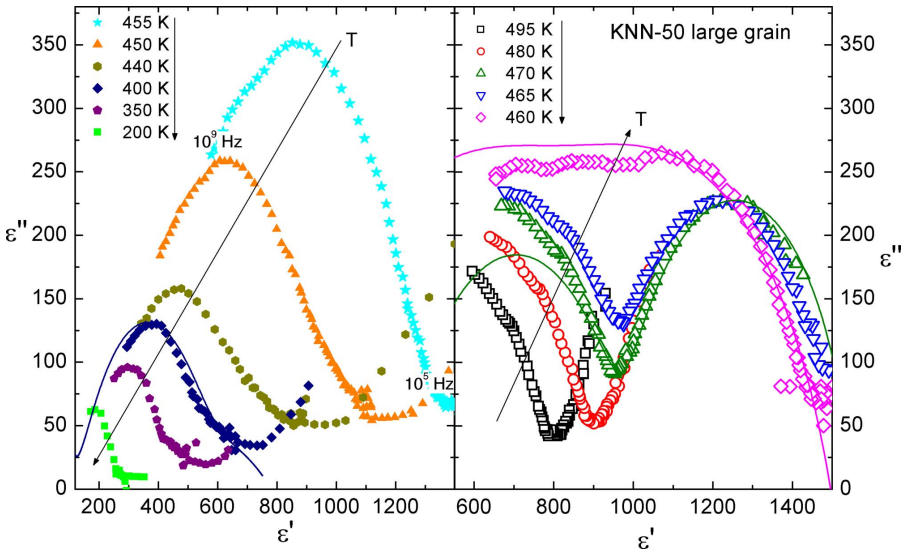

FIG. 7. (Color online) Cole–Cole plot of the dielectric spectra of large-grain KNN-50 at different temperatures in the frequency range 10^5–10^9 Hz. Symbols—experiment; lines—fits with Eq. (3). The arrows denote the cooling direction.

kHz. At high temperatures in the cubic paraelectric phase, there is an overdamped THz mode which partially softens and explains essentially the low-frequency permittivity, except probably its strong peak near T_{C1}. No microwave data are unfortunately available in this temperature range. On cooling, a relaxation of the mean frequency ν_1 in the 1–50 GHz range appears in the tetragonal ferroelectric phase, as is common in other ferroelectric perovskites.[23] However, unlike most other ferroelectric ceramics, another relaxation with the lower frequency ν_2 in the 10–100 MHz range is also present in the whole temperature range. Due to our experimental limitation, we could study both of them only below 500 K.

The mode in the THz range behaves like the central mode seen in many ferroelectrics.[23] Recently Hlinka *et al.*[20] revealed an overdamped oscillator in the THz range (fitted quite well to a Debye relaxation) distinctly below the polar phonons in the tetragonal $BaTiO_3$ in the response parallel to P_s, which was assigned to hopping of the off-centered Ti ions between the lower and higher-energy off-centered sites (its reciprocal frequency corresponds to the short dwell time in these higher-energy sites). In the same frequency range also, the hopping and vibrations of Ti ions perpendicular to P_s (central+soft mode of E symmetry) appear. Similar model could be applied to $KNbO_3$, and in extension to KNN-50. The hopping of the off-centered Nb ions then corresponds to the overdamped THz excitation. The jumpwise increase of its frequency in the rhombohedral phase and gradual vanishing of its dielectric strength confirm its link to the dynamic dis-

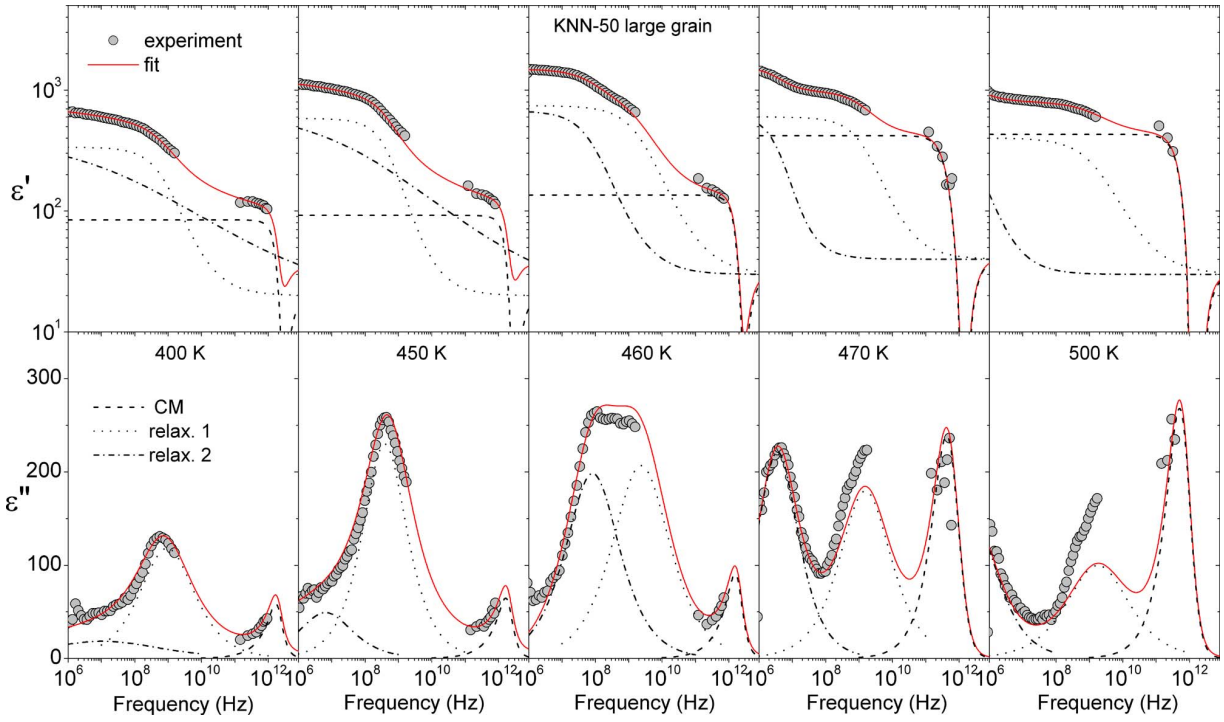

FIG. 8. (Color online) Dielectric permittivity (ε') and loss (ε'') of the large-grain KNN-50 at selected temperatures around the tetragonal-orthorhombic PT. Circles—experimental data; solid lines—fits with Eq. (3); dashed lines—separated dielectric contributions.

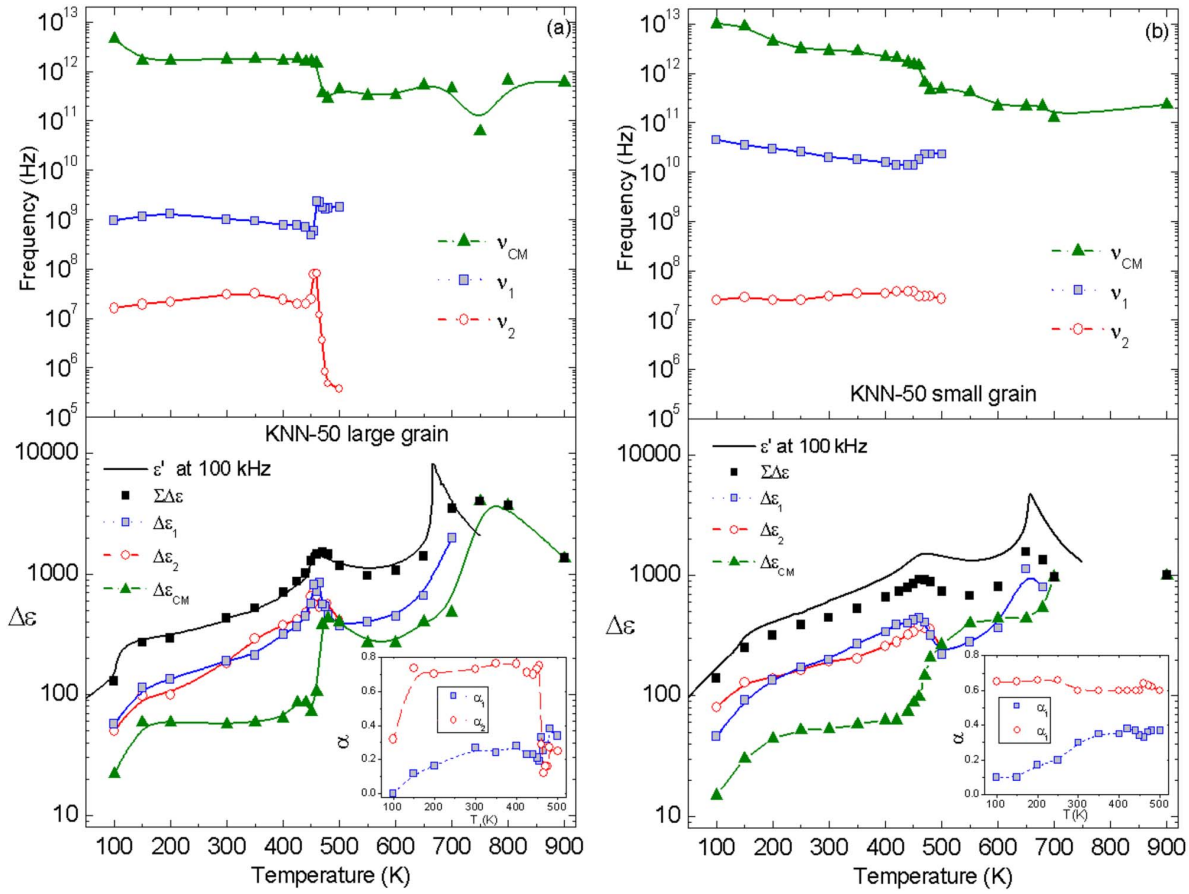

FIG. 9. (Color online) Temperature dependences of the frequencies and dielectric contributions of the soft mode and relaxations in KNN-50 ceramics with large (a) and small (b) grains.

order of Nb ions, which should gradually disappear in the rhombohedral phase according to the eight-site disorder model.

The difficult question that remains is the origin of the two relaxation regions at lower frequencies. It appears to be a general feature in perovskite ceramics that they show a relaxational dispersion below phonons in their ferroelectric phases.[24–27] Its origin is quantitatively not well understood because at least two different mechanisms can be the cause: piezoelectric resonances within the grains and oscillations of ferroelectric domain walls. Moreover, since some of the ferroelectric domains in perovskites are also ferroelastic, their oscillation can emit acoustic waves which determine the eigenfrequencies of these oscillations. Recently Porokhonsky *et al.*[28] revealed that in $Pb(Zr,Ti)O_3$ (PZT) ceramics the dispersion in the MHz to gigahertz (GHz) range can be separated in two contributions. The lower-frequency contribution in the 10^8 Hz range corresponds to piezoelectric resonances within grains; therefore, its frequency increases with decreasing grain size. The higher-frequency and stronger relaxation in the 10^9 Hz range, which was suppressed by poling the ceramics, should correspond to ferroelectric (probably also ferroelastic) domain-wall oscillations. In our case, smaller grains should display finer domain structure which results in their faster dynamics.

Let us compare the mean frequencies of the three dispersions, which contribute to the permittivity in our two KNN-50 ceramics. The THz mode has slightly higher frequency in the small-grain sample. This can be understood as an effect of low-permittivity grain boundaries (dead layers), as observed in $SrTiO_3$ (Refs. 29 and 30) and $BaTiO_3$ (Ref. 31) ceramics. In this case the grain boundaries in the small-grain sample enhance more the effective soft-mode–central-mode frequency than in the large-grain sample due to stronger depolarization field effects from the grain boundaries. This also agrees with the smaller permittivity of the small-grain ceramics in the cubic phase.

The ν_1 relaxation frequency below T_{C2} appears to be about 20 times higher in the small-grain sample. This is just the ratio of the grain sizes in both ceramics; therefore, it could be appealing to relate it to piezoelectric resonances within the grains. However, we should consider the existence of ferroelastic domains, which produce stronger effects due to oscillations of ferroelastic-ferroelectric domain walls. This mechanism was analyzed by Arlt *et al.*,[25] who suggested that the GHz relaxation in $BaTiO_3$ ceramics is due to the oscillating sets of laminar ferroelastic domain walls, which emit transverse acoustic waves. Its frequency $\nu_0 = \sqrt{c_{55}^*/\rho}/\pi d$ is inversely proportional to the width of the domains d, where c_{55} is the shear elastic constant and ρ is the sample density. The domain width is usually related to the grain size g in the way $d \propto (g)^{1/2}$ for the grain sizes at least between 1 and 10 μm.[32] In analogy with $BaTiO_3$ and PZT ceramics, we may suppose that even in the small-grain sample still few

domains remain in a single grain. Then the domain size ratio between both samples $d_{LG}/d_{SG} \sim (g_{LG})^{1/2}/d_{SG}$—where LG stands for large-grain and SG stands for small-grain samples, respectively—would be 6.3 for the case of single domain grains in the small grain-sample or higher, and the frequency of domain-wall oscillations should be at least six times higher in the small-grain sample in the tetragonal phase. It appears that the size difference of ferroelastic domains between the two ceramics is much higher. For the particular case of three domains in the small grains, d_{SG} is 0.16 and the domain size ratio becomes almost 19. From Fig. 9 we see that the experimental ratio between the frequencies below T_{C2} is $\nu_{1SG}/\nu_{1LG} \sim 19$ [$\nu_{1LG}(300\ K) \sim 1$ GHz, $\nu_{1SG}(300\ K) \sim 19$ GHz]. Unfortunately, we have no data about the domain structure in our samples. Nevertheless, it is at least clear that the domain structure in the tetragonal and orthorhombic phases should differ appreciably, the domain structure in the orthorhombic phase being much more complicated. It is interesting to note that the dielectric contribution $\Delta\varepsilon_1$ as well as the distribution of the relaxations frequencies ($\alpha_1 \sim 0.2$) are nearly independent of the grain size [$\Delta\varepsilon_{1LG}(300\ K)=190$, $\Delta\varepsilon_{1SG}(300\ K)=200$, see Fig. 9], except for temperatures closely around T_{C2}.

The lower-frequency relaxation is affected by the grain size in a different way. In the small-grain sample, the distribution of the relaxation frequencies is quite broad (Cole–Cole parameter $\alpha_2 \sim 0.6$). The mean frequency lies in the MHz range, but its estimation is difficult because another broad dispersion at lower frequencies (below 100 Hz) affects our data. We see a monotonous weak roughly logarithmic increase in ε' down to 100 Hz without any sign of saturation, which is accompanied by a frequency independent loss spectra (constant-loss spectrum or 1/f noise as in relaxor ferroelectrics below the freezing temperature).[33] In the large-grain sample above T_{C2}, this relaxation is quite narrow ($\alpha_2 \sim 0.2$), but below T_{C2} it suddenly broadens (up to $\alpha_2 \sim 0.7$, see the insets of Fig. 9). In analogy to relaxors, we could relate this dispersion to some domain breathing with a very broad distribution of activation energies for the domain-wall oscillations (displacements). Let us note that there are more types of ferroelectric domains in the orthorhombic ceramics and in principle, all of them could contribute to the permittivity dispersion. Particularly the nonferroelastic (180° ferroelectric) domains can contribute and their characteristic frequencies of breathing are determined by pinning of domain walls on defects or grain boundaries, which can produce a very broad distribution of characteristic frequencies. Therefore, we could speculate that our broad lower-frequency relaxation is due to nonferroelastic domain-wall oscillations. However, an optional assignment of microwave dielectric dispersions in disordered perovskite systems appeared quite recently. Molecular dynamics simulation based on first-principles atomistic approach in 0.75PMN-0.25PT by Grinberg *et al.*[34] have shown that GHz relaxational dispersion below polar phonon response may appear in the dielectric response of such a system just due to random fields of locally spatially fluctuating neighboring ions, without any need of mesoscopic or macroscopic inhomogeneities (polar nanoregions and domains) in the system. To check the validity of such interpretation, it would be challenging to study the microwave dielectric response in a single crystalline single domain sample.

In summary, we have assigned the strong dielectric dispersion in the MHz to GHz range of our KNN-50 ceramics and its pronounced temperature and grain-size dependence to dynamics of ferroelastic and nonferroelastic but ferroelectric domains. No quantitative understanding of the effects is possible without knowledge of the domain structure in the ceramics. More information could be achieved by similar investigation on poled samples, which could eliminate or reduce the effect of domains.

V. CONCLUSIONS

KNN-50 ceramics with two different grain sizes (10 and 0.5 μm) were studied by DSC and broad-band dielectric spectroscopy. Three PTs from the paraelectric cubic phase to the ferroelectric tetragonal, orthorhombic, and rhombohedral phases were detected in both samples. The small-grain sample shows smaller permittivity in the cubic phase and more smeared PTs.

An overdamped mode was revealed in both samples in the THz range, related to the hopping+oscillations of the off-centered Nb ions in a multiwell potential. This mode loses its strength at each PT and jumpwise increases its frequency on cooling down to the rhombohedral phase where the dynamic disorder (Nb-hopping) vanishes.

Two additional relaxation regions appear in the MHz to GHz range in the ferroelectric phases. The higher one in the GHz range is strongly dependent on the grain size, but we assign it to laminar ferroelastic domain-wall dynamics, which should contribute to the dielectric response more strongly than the piezoelectric resonances on the grains. The lower-frequency relaxation is broader and we assign it tentatively to 180° ferroelectric domain-wall dynamics. However, details of the strong and striking temperature dependence particularly near the tetragonal-orthorhombic PT are not well understood.

ACKNOWLEDGMENTS

This work was supported by the Academy of Sciences of the Czech Republic (Project Nos. IAA100100701, AVOZ10100520, and KJB100100704), the Czech Ministry of Education (Project No. OC101-COST 539), the Grant Agency of the Czech Republic (Project No. 202/06/0403), and the Swedish Research Council (Grant No. 621-2008-5730). The authors thank Dr. Guanghua Liu for his technical assistances on SEM characterization.

[1] G. Shirane, R. Newnham, and R. Pepinsky, Phys. Rev. **96**, 581 (1954).
[2] E. Wiesendanger, Ferroelectrics **6**, 263 (1974).
[3] L. A. Reznitchenko, A. V. Turik, E. M. Kuznetsova, and V. P. Sakhnenko, J. Phys.: Condens. Matter **13**, 3875 (2001).
[4] R. P. Herber and G. A. Schneider, Appl. Phys. Lett. **90**, 252905 (2007).
[5] A. Ahtee and A. M. Glazer, Acta Crystallogr., Sect. A: Cryst. Phys., Diffr., Theor. Gen. Crystallogr. **32**, 434 (1976).
[6] M. D. Fontana, G. Metrat, J. L. Servoin, and F. Gervais, J. Phys. C **17**, 483 (1984).
[7] M. D. Fontana, G. E. Kugel, G. Metrat, and C. Carabatos, Phys. Status Solidi B **103**, 211 (1981).

[8]Ph. Pruzan, D. Gourdan, and J. C. Chervin, Phase Transitions **80**, 1103 (2007).
[9]R. J. C. Lima, W. Paraguassu, P. T. C. Freire, J. M. Sasaki, F. E. A. Melo, J. Mendes Filho, and S. Lanfredi, J. Raman Spectrosc. **36**, 28 (2005).
[10]Y. Shiratori, A. Magrez, and C. Pithan, Chem. Phys. Lett. **391**, 288 (2004).
[11]E. Buixaderas, D. Nuzhnyy, I. Gregora, S. Kamba, B. Malic, and M. Kosec, Ferroelectrics **391**, 51 (2009).
[12]E. Buixaderas, D. Nuzhnyy, I. Gregora, S. Kamba, M. Berta, B. Malic, and M. Kosec, IEEE Trans. Ultrason. Ferroelectr. Freq. Control **56**, 1843 (2009).
[13]V. Lingwal, B. S. Semwal, and N. S. Panwal, Bull. Mater. Sci. **26**, 619 (2003).
[14]M. P. McNeal, S.-J. Jang, and R. E. Newnham, J. Appl. Phys. **83**, 3288 (1998).
[15]M. Eriksson, H. Yan, M. Nygren, M. Reece, and Z. Shen, "Low temperature consolidated lead-free ferroelectric niobate ceramics with improved electrical properties", J. Mater. Res. (in press).
[16]J. Krupka, T. Zychowicz, V. Bovtun, and S. Veljko, IEEE Trans. Ultrason. Ferroelectr. Freq. Control **53**, 1883 (2006).
[17]F. Gervais, *Infrared and Millimeter Waves*, edited by K. J. Button, (Academic, New York, 1983), Vol. 8, p. 279.
[18]M. D. Fontana, A. Ridah, G. E. Kugel, and C. Carabatos-Nedelec, J. Phys. C **21**, 5853 (1988).
[19]Y. Girshberg and Y. Yakoby, Solid State Commun. **103**, 425 (1997).
[20]J. Hlinka, T. Ostapchuk, D. Nuzhnyy, J. Petzelt, P. Kuzel, F. Kadlec, C. Kadlec, P. Vanek, I. Ponomareva, and L. Bellaiche, Phys. Rev. Lett. **101**, 167402 (2008).
[21]R. Comès, M. Lambert, and A. Guinier, Acta Crystallogr., Sect. A: Cryst. Phys., Diffr., Theor. Gen. Crystallogr. **26**, 244 (1970).
[22]V. A. Shuvaeva, K. Yanagi, K. Yagi, K. Sakaue, and H. Terauchi, Solid State Commun. **106**, 335 (1998).
[23]E. Buixaderas, S. Kamba, and J. Petzelt, Ferroelectrics **308**, 131 (2004).
[24]C. Kittel, Phys. Rev. **83**, 458 (1951).
[25]R. Clemens, G. Luther, and H. E. Müser, Phys. Status Solidi A **64**, 637 (1981).
[26]N. A. Pertsev and G. Arlt, J. Appl. Phys. **74**, 4105 (1993).
[27]G. Arlt, U. Bottger, and S. Witte, Ann. Phys. **506**, 578 (1994).
[28]V. Porokhonskyy, L. Jin, and D. Damjanovic, Appl. Phys. Lett. **94**, 212906 (2009).
[29]J. Petzelt, T. Ostapchuk, I. Gregora, D. Nuzhnyy, I. Rychetsky, K. Maca, and Z. Shen, Ferroelectrics **363**, 227 (2008).
[30]J. Petzelt, T. Ostapchuk, I. Gregora, P. Kuzel, J. Liu, and Z. Shen, J. Phys.: Condens. Matter **19**, 196222 (2007).
[31]T. Ostapchuk, J. Petzelt, M. Savinov, V. Buscaglia, and L. Mitoseriu, Phase Transitions **79**, 361 (2006).
[32]G. Arlt, Ferroelectrics **104**, 217 (1990).
[33]I. Rychetský, S. Kamba, V. Porokhonskyy, A. Pashkin, M. Savinov, V. Bovtun, J. Petzelt, M. Kosec, and M. Dressel, J. Phys.: Condens. Matter **15**, 6017 (2003).
[34]I. Grinberg, Y.-H. Shin, and A. M. Rappe, Phys. Rev. Lett. **103**, 197601 (2009).